An $[Fe^{III}_{34}]$ molecular metal oxide

Alice E. Dearle, Daniel J. Cutler, Hector W. L. Fraser, Sergio Sanz, Edward Lee, Sourav Dey, Ismael F. Diaz-Ortega, Gary S. Nichol, Hiroyuki Nojiri, Marco Evangelisti, Gopalan Rajaraman*, Jürgen Schnack,* Leroy Cronin, and Euan K. Brechin*

Affiliations

Ms A. Dearle, Dr S. Sanz, Mr H. Fraser, Mr. D. J. Cutler, Mr E. Lee, Dr. G. S. Nichol, Prof. E. K. Brechin, EaStCHEM School of Chemistry, The University of Edinburgh, David Brewster Road, Edinburgh, EH93FJ, UK. E-mail: E.Brechin@ed.ac.uk

Mr E. Lee, Prof. L. Cronin, WestCHEM School of Chemistry, The University of Glasgow, University Avenue, Glasgow, G12 8QQ, UK. E-mail: Lee.Cronin@glasgow.ac.uk

Mr S. Dey, Prof. G. Rajaraman, Department of Chemistry, Indian Institute of Technology Bombay, Mumbai, 400076, India. Email: rajaraman@chem.iitb.ac.in

Dr. I. F. Diaz-Ortega, Prof. H. Nojiri, IMR, Tohoku Univ, Katahira 2-1-1, Aobaku, Sendai, 980-8577, Japan. Email: nojiri@imr.tohoku.ac.jp

Dr M. Evangelisti. Instituto de Ciencia de Materiales de Aragón, CSIC-Universidad de Zaragoza, 50009 Zaragoza, Spain. Email: evange@unizar.es

Prof. J. Schnack, Fakultät für Physik, Universitat Bielefeld, Postfach 100131, D-33501 Bielefeld, Germany. Email: jschnack@uni-bielefeld.de

Abstract

The dissolution of anhydrous iron bromide in a mixture of pyridine and acetonitrile, in the presence of an organic amine, results in the formation of an $[Fe_{34}]$ metal oxide molecule, structurally characterized by alternate layers of tetrahedral and octahedral Fe(III) ions connected by oxide and hydroxide ions. The outer shell of the cage is capped by a combination of pyridine molecules and bromide ions. Magnetic data, measured at temperatures as low as 0.4 K and fields up to 35 T, reveal competing antiferromagnetic exchange interactions; DFT calculations showing that the magnitudes of the coupling constants are highly dependent on both the Fe-O-Fe angles and Fe-O distances. The simplicity of the synthetic methodology, and the structural similarity between $[Fe_{34}]$, iron oxides, previous Fe(III)-oxo cages, and polyoxometalates (POMs), hints that much larger, molecular Fe(III) oxides can be made.

Introduction

It is interesting to note the enormous size difference between the largest polyoxometalates (POMs), most commonly constructed from high oxidation state, diamagnetic metal ions,[1] and cages built from the high spin (d^5), paramagnetic Fe(III) ion,[2] despite both often containing similar metal oxide cores.[3] The most pertinent examples of Fe(III) cages conforming to POM-like architectures are $[Fe_{13}]$[4] and $[Fe_{17}]$;[5] both are structurally related with alternating layers/shells of tetrahedral and octahedral metal ions - the former has the α-Keggin structure,[4a] and the latter the ε-Keggin structure with four additional capping metal ions.[5] In addition, the much studied $[Fe^{III}_{30}]$ icosidodecahedron,[6] demonstrates that very large (heterometallic) molecular metal oxides containing paramagnetic metal ions can (a) be synthesized, (b) retain POM-like architectures, and (c) possess fascinating physical

properties - the high symmetry icosidodecahedron possessing geometric spin frustration.[7] This has prompted us to speculate that large and very large Fe(III) molecular metal oxides, approaching the size and structural diversity of POMs, can be constructed, but with the terminal oxides replaced by simple monodentate ligands. There appears to be no chemical reason why such species cannot form, and their synthesis would help bridge the 'gap' between the fields of molecular magnetism (where the vast majority of molecules have nuclearities less than twenty) and POM chemistry (where complexes can be an order of magnitude larger), producing species with a myriad of potentially interesting physical properties, with applications in chemistry, physics, materials science, biology and medicine.[8]

The $[Fe_{17}]$ cage in particular hints at a potentially successful route to the synthesis of such species. It is made very simply by dissolving anhydrous FeX_3 (X = Cl, Br) in wet pyridine (or any analogous liquid base such as β-picoline, iso-quinoline, ethyl-pyridine, lutidine, *etc*).[9] The pyridine appears to fulfill at least five simultaneous roles: it is the solvent, the base, the source of water (hence oxide), monodentate ligand (with the halide ions) that encases the metal oxide core, and source of the charge balancing pyridinium cations. Interestingly, in POM chemistry the addition of (bulky) organic amine cations is thought to aid the self-asembly of large nuclearity species by isolating the smaller building blocks, preventing rapid aggregation into complexes with (smaller) stable spherical topologies.[10] Herein we discuss the synthesis, structure and magnetic behaviour of $[Fe^{III}_{34}(\mu_4\text{-}O)_4(\mu_3\text{-}O)_{34}(\mu_2\text{-}OH)_{12}Br_{12}(py)_{18}]Br_2$ (**1**) (Figure 1, S1-S6) which is made via just such a strategy, through a small modification (the addition of either hexamethylene tetramine (HMTA) or morpholine) in the preparation of $[Fe_{17}]$.[11]

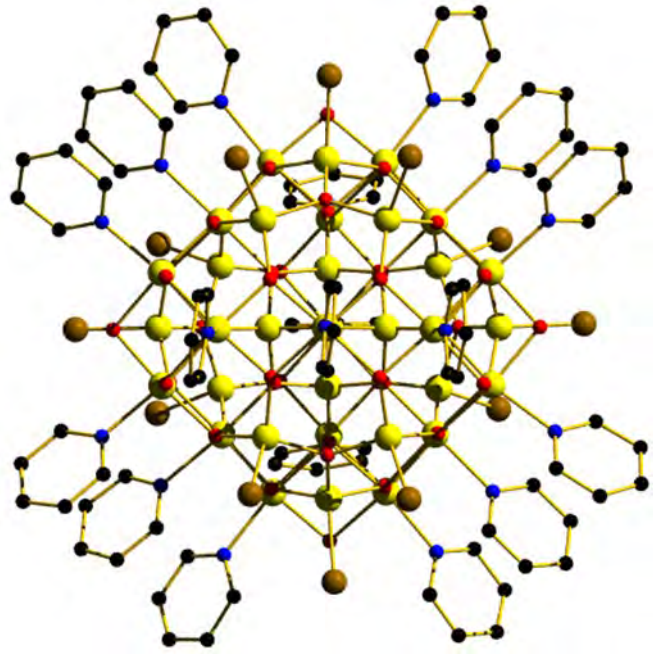

Figure 1. Molecular structure of the cation of **1**. Colour code: Fe = yellow, O = red, N = blue, C = black, Br = brown. H atoms and anions omitted for clarity.

Results and Discussion

Compound **1**, crystallizes in the monoclinic space group $P2_1/n$ with the full complex in the asymmetric unit. The metallic skeleton (Figure 2, S2-S3) describes a $[Fe^{III}_4]$ tetrahedron encapsulated within a $[Fe^{III}_{18}]$ truncated tetrahedron, whose large faces are capped by $[Fe^{III}_3]$ triangles. The (sixteen) metal ions in the inner tetrahedron and the outer triangles are all tetrahedral and the (eighteen) Fe ions in

the truncated tetrahedron are all octahedral. The presence of tetrahedral-octahedral-tetrahedral "shells" of metal ions is as found in the [Fe_{13}] and [Fe_{17}] cages (Figure 3) and Fe containing minerals such as magnetite and maghemite. The inner tetrahedron is connected to the [Fe^{III}_{18}] truncated tetrahedron *via* ten (4 x μ_4; 6 x μ_3) O^{2-} ions (Figure S2). Each face-capping, oxo-centered [Fe_3] triangle is connected to the [Fe^{III}_{18}] truncated tetrahedron *via* six μ_3-O^{2-} ions. The remaining twelve μ_2-OH^- ions link the metal ions situated on the triangular faces on the truncated tetrahedron. Each of the octahedral metal ions in the [Fe_{18}] truncated tetrahedron and tetrahedral metal ions in the face capping [Fe_3] triangles have their coordination geometries completed through the presence of a pyridine (py) molecule and a bromide, respectively. The Br counter anions are associated with the triangular faces of the truncated tetrahedron with Br···(μ_2-)O distances in the range ~3.21-3.48 Å, and the py C-atoms on a neighbouring molecule (Br···C, ~3.46 Å). The other prevalent intermolecular interactions occur between adjacent Br ions and py molecules (Br···C, ~3.50 Å).

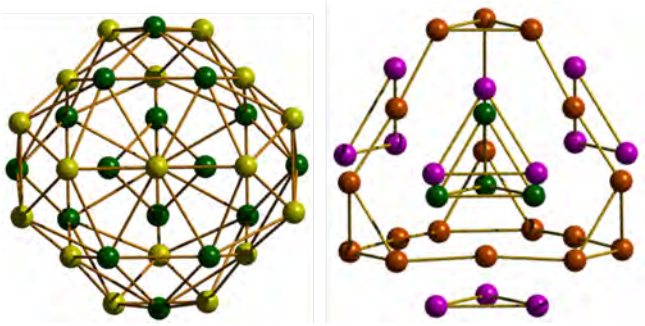

Figure 2. Alternative views of the metallic skeleton of **1**. Left: highlighting the layers of tetrahedral (green) and octahedral (yellow) metal ions. Right: highlighting the central [Fe_4] tetrahedron (green) encapsulated by the [Fe_{18}] truncated tetrahedron (brown) whose large faces are capped by [Fe_3] triangles (pink).

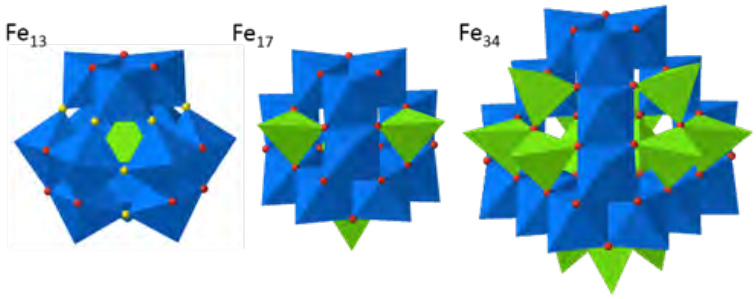

Figure 3. Polyhedral representation comparing [Fe_{13}] (left),[4a] [Fe_{17}] (centre)[5] and [Fe_{34}] (right). Tetrahedral Fe(III) = green, octahedral Fe(III) = blue. The F ions in [Fe_{13}] are shown in yellow.

Magnetic measurements of **1** strongly hint at rather large, competing, antiferromagnetic exchange interactions between the Fe centres. The susceptibility data (T = 350 – 2 K, B = 0.1 T; Figure 4a) shows that the χT value at T = 350 K (~75 cm^3 K mol^{-1}) is well below the Curie constant expected for thirty four uncoupled Fe(III) ions (150 cm^3 K mol^{-1}). As temperature is decreased the value of χT first increaes to a broad maximum of ~95 cm^3 K mol^{-1} centred around T = 150 K, before dropping slowly to a value of ~90 cm^3 K mol^{-1} at T = 50 K. Below this temperature the value drops significantly, and is strongly field dependent. Magnetisation (M) data (Figure 4b) show an initial, fairly rapid, increase to a value of ~12 μ_B (for T = 2 K, B < 2 T) before first plateauing and then increasing in a more linear fashion to B = 7 T where $M \approx 15\ \mu_B$. This linear like increase is continued in the B = 7-35 T field range (Figure 4c), where M reacheas a maximum value of ~40 μ_B. The low temperature susceptibility and magnetisaton

data suggest a relatively small magnetic moment, in agreement with heat capacity measurements where the zero-field magnetic entropy content reaches just S = 1.6 R at T = 2 K (Figure S7).

A simple explanation of the temperature and field dependence of the magnetic data is not straightforward. Since the cluster is much too large for a quantum calculation in a spin model such as the Heisenberg model we resort to two approximations. Classical Monte Carlo calculations (CMC) of a classical Heisenberg model, that often deliver accurate results in the temperature and field regions where quantum effects are of minor importance, *i.e.* at elevated temperatures compared to the exchange couplings,[7(a)] suggest an even smaller susceptibility and magnetization compared to the experiment, when using the exchange parameters provided by DFT (see Table 1 below). In view of the relatively strong exchange, we surmise that we are always in the quantum regime, where the classical calculations point us in the right direction, but are poor approximations otherwise. Guided by the nearly flat high temperature χT data, we investigated a quantum model where we assume a low-lying level structure similar to a zero-field split total spin S = 11 with g fixed at g = 2.04, as obtained from HFEPR measurements (Figure S8). This effective model fits both χT vs T and M vs B (Figs. 4a and 4b) astonishingly well, and it also explains why specific heat measurements detect very few low-lying levels (compared to a total of 2.8×10^{26} levels). While the absolute numbers in this effective model should be taken with a pinch of salt, they do hint at the presence of non-neglibile anisotropy. We also expect that the true low-energy spectrum contains numerous additional (small) spin states, and in the absence of any out-of-phase χ'' signals in the ac susceptibility, that may not be of perfect easy axis character.

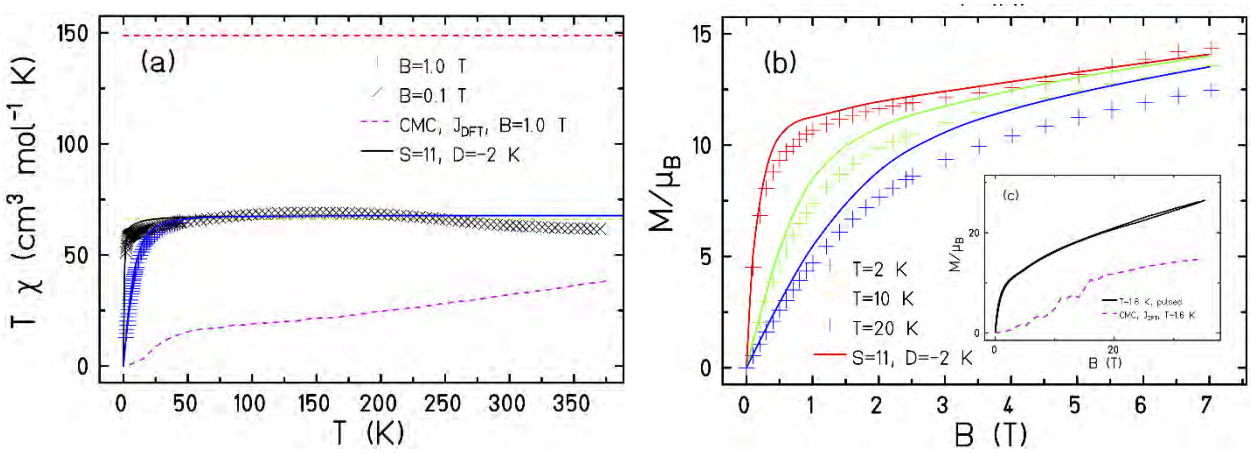

Figure 4. (a) Magnetic susceptibility: symbols denote measurements, the red dashed line marks the paramagnetic limit for 34 S = 5/2, the green dashed line the respective value for S = 11. The solid curves belong to single-spin calculations, the dashed magenta curve to CMC simulations. (b) Low-field magnetization: the solid curves depict the single-spin magnetization. (c) Pulsed-field magnetisation (solid curve) compared to (b) and CMC.

In order to estimate the magnetic exchange interactions in **1** we have employed a DFT methodology (B3LYP/TZVP) known to yield excellent numerical estimates of J values.[12],[13],[14],[15] Calculations were performed using the model structures shown in Figures S9-S13 (see computational details in ESI for discussion). The symmetric nature of the cage reduces the number of unique exchange interactions to five, describing those between: (i) inner tetrahedral Fe(III) ions (J_1) connected by μ_3-O^{2-} ions; (ii) inner tetrahedral and outer octahedral Fe(III) ions (J_2) connected by μ_3/μ_4-O^{2-} ions; (iii) outer octahedral Fe(III) ions (J_3) connected by μ_3-O^{2-} ions; (iv) outer tetrahedral Fe(III) ions (J_4) connected by

μ_3-O^{2-} ions; and (v) outer tetrahedral and outer octahedral Fe(III) ions (J_5) connected by μ_3-O^{2-} ions (Scheme S1). The calculated *J* values are listed in Table 1. The computed exchange coupling constants are all antiferromagnetic in nature and strongly correlated to the Fe-O distances and Fe-O-Fe angles, with larger angles enhancing the antiferromagnetic part of the exchange, in agreement with the magneto-structural correlation developed by Weihe and Güdel.[16] Spin density data are provided in Figures S14-S18 and Tables S2-S6. We have computed the overlap integrals for all *J* pairs (Tables S7-S11), which show a direct correlation between the number of orbital interactions and the magnitude of the antiferromagnetic exchange. For example, for J_3 only two dominant overlaps ($d_{xy}||d_{xy}$ and $d_{x2-y2}||d_{xy}$) are detected leading to the smallest calculated *J* value (-15.7 cm^{-1}), whereas there are seven different, large interactions for J_5, resulting in the largest *J* value (-68.2 cm^{-1}). Note that in the latter, the d_{xz} orbital of tetrahedral Fe(III) ion is found to overlap significantly with all the d-orbitals of octahedral Fe(III) ion, with the exception of the d_{xy} orbital.

	Fe-O-Fe (°)	Fe-O (Å)	Fe···Fe (Å)	J_{DFT}(cm^{-1})
J_1	118	1.86	3.19	-24.2
J_2	121	1.95	3.39	-38.4
J_3	95.5	1.97	2.92	-15.7
J_4	119	1.92	3.32	-47.3
J_5	129	1.92	3.47	-68.2

Table 1. Calculated J_{DFT} values for the five unique exchange interactions in **1**, alongside the average Fe-O-Fe angles and Fe-O, Fe···Fe distances per interaction.

Conclusions

The addition of an organic amine (HMTA, morpholine) to a py/MeCN solution of $FeBr_3$ produces an [Fe^{III}_{34}] complex, double the size of the cage produced in py/MeCN alone, [Fe^{III}_{17}]. The molecule, whose structure describes an [Fe_4] tetrahedron encapsulated in a [Fe_{18}] truncated tetrahedron, face-capped by four [Fe_3] triangles, is characterized by alternate layers of tetrahedral and octahedral Fe ions linked by oxide and hydroxide anions. Magnetic measurements reveal strong AF exchange interactions between the Fe(III) ions, with DFT calculations suggesting a direct correlation between the number of orbital interactions and the magnitude of the AF exchange. The simplicity of the synthetic procedure and the structural similary of [Fe_{34}] to much larger POMs of high oxidation state, diamagnetic metal ions such as V, W and Mo, hints that a diverse family of novel Fe(III) molecular metal oxide structures awaits discovery. This, in turn, suggests an exciting route to the bottom-up formation of metal oxide 'nanoparticles' and a raft of potential applications.

Acknowledgements

EKB thanks the EPSRC for funding (grants EP/N01331X/1 and EP/P025986/1). GR thanks UGC-UKIERI grant number 184-1/2018(IC) and SERB (CRG/2018/000430). SD thanks the UGC for an SRF fellowship. ME thanks MINECO (RTI2018-094909-J-I00). JS thanks the Deutsche Forschungsgemeinschaft DFG (314331397 (SCHN 615/23-1).

Keywords: Fe(III) cages • molecular metal oxides • magnetic behaviour • spin frustration • DFT

References

[1] a) A. Müller, E. Beckmann, H. Bögge, M. Schmidtmann, A. Dress*, Angew. Chem. Int. Ed*. **2002**, *41*, 1162-1167; A. Müller, E. Krickemeyer, J. Meyer, H. Bögge, F. Peters, W. Plass, E. Diemann, S. Dillinger, F. Nonnenbruch, M. Randerath, C. Menke, *Angew. Chem. Int. Ed.* **1995**, *34*, 2122-2124; c) N. I. Gumerova, A. Rompel, *Nat. Rev. Chem*. **2018**, *2*, 0112.

[2] The three largest Fe(III) cages known are [Fe_{42}], [Fe_{60}] and [Fe_{64}], although none contain metal-oxo cores. The first is built with cyanide, the second tripodal alcohols, and the third a combination of triethanolamine and carboxylate: a) S. Kang, H. Zheng, T. Liu, K. Hamachi, S. Kanegawa, K. Sugimoto, Y. Shiota, S. Hayami, M. Mito, T. Nakamura, M. Nakano, M. L. Baker, H. Nojiri, K. Yoshizawa, C. Duan, O. Sato, *Nat. Commun*. **2015**, *6*, 5955; b) J.-R. Jiménez, A. Mondal, L.-M. Chamoreau, P. Fertey, F. Tuna, M. Julve, A. Bousseksou, R. Lescouëzec, L. Lisnard, *Dalton Trans*. **2016**, *45*, 17610−17615; c) T. Liu, Y.-J. Zhang, Z. M. Wang, S. Gao, *J. Am. Chem. Soc.* **2008**,*130*, 10500−10501.

[3] For examples of Fe(III) cages with metal-oxo cores see, for example: a) D. Low, L. F. Jones, A. Bell, E. K. Brechin, T. Mallah, E. Rivière, S. J. Teat, E. J. L. McInnes, *Angew. Chem., Int. Ed*. **2003**, *42*, 3781−3784, b) O. Nachtigall, M. Kusserow, R. Clérac, W. Wernsdorfer, M. Menzel, F. Renz, J. Mrozinski, J. Spandl, *Angew. Chem. Int. Ed.* **2015**, *54*, 10361-10364.

[4] a) A. Bino, M. Ardon, D. Lee, B. Spingler, S. J. Lippard, *J. Am. Chem. Soc*. **2002**, *124*, 4578−4579; b) J. van Slageren, P. Rosa, A. Caneschi, R. Sessoli, H. Casellas, Y. V. Rakitin, L. Cianchi, F. Del Giallo, G. Spina, A. Bino, A.-L. Barra, T. Guidi, S. Carretta, R. Caciuffo, *Phys. Rev. B* **2006**, *73*, 014422; c) O. Sadeghi, L. N. Zakharov, M. Nyman, *Science*, **2015**, 347, 1359-1362; d) O. Sadeghi, C. Falaise, P. I. Molina, R. Hufschmid, C. F. Campana, B. C. Noll, N. D. Browning, M. Nyman, *Inorg. Chem*. **2016**, 55, 11078−11088; e) N. A. G. Bandeira, O. Sadeghi, T. J. Woods, Y.-Z. Zhang, J. Schnack, K. R. Dunbar, M. Nyman, C. Bo, *J. Phys. Chem. A* **2017**, 121 1310-1318.

[5] a) G. W. Powell, H. N. Lancashire, E. K. Brechin, D. Collison, S. L. Heath, T. Mallah, W. Wernsdorfer, *Angew. Chem. Int. Ed*. **2004**, *43*, 5772−5775; b) C. Vecchini, D. H. Ryan, L. M. D. Cranswick, M. Evangelisti, W. Kockelmann, P. G. Radaelli, A. Candini, M. Affronte, I. A. Gass, E. K. Brechin, O. Moze, *Phys. Rev. B* **2008**, *77*, 224403; M. Evangelisti, A. Candini, A. Ghirri, M. Affronte, G. W. Powell, I. A. Gass, P. A. Wood, S. Parsons, E. K. Brechin, D. Collison, S. L. Heath, *Phys. Rev. Lett*. **2006**, *97*, 167202

[6] V. O. Garlea, S. E. Nagler, J. L. Zarestky, C Stassis, D. Vaknin, P. Kögerler, D. F. McMorrow, C. Niedermayer, D. A. Tennant, B. Lake, Y. Qiu, M. Exler, J. Schnack, M. Luban, *Phys. Rev. B* **2006**, *73*, 024414.

[7] a) A. Müller, M. Luban, C. Schröder, R. Modler, P. Kögerler, M. Axenovich, J. Schnack, P.C. Canfield, S. Bud'ko, and Neil Harrison, *ChemPhysChem* **2001**, 2, 517-521; b) J. Schnack, *Dalton Trans*. **2010**, *39*, 4677−4686.

[8] a) D. L. Long, E. Burkholder, L. Cronin, *Chem. Soc. Rev*. **2007**, *36*, 105–121; b) D. L. Long, R. Tsunashima, L. Cronin, *Angew. Chem. Int. Ed*. **2010**, *49*, 1736–1758; c) M. T. Pope, *Heteropoly and Isopoly Oxometalates; Springer-Verlag*, New York, **1983**; d) A.Müller, S. Roy, in *The Chemistry of Nanomaterials:Synthesis, Properties and Applications*, ed. C. N. R. Rao, A. Müller, A. K. Cheetham, Wiley-VCH, Weinheim, **2004**.

[9] I. A. Gass, C. J. Milios, M. Evangelisti, S. L. Heath, D. Collison, S. Parsons, E. K. Brechin, *Polyhedron*, **2007**, 26, 1835-1837.

[10] M. Hutin, M. H. Rosnes, D.-L. Long, L. Cronin, *Comprehensive Inorganic Chemistry II*, **2013**, 2, 241-269.

[11] Experimental and crystallographic details can be found in the SI.

[12] E. Ruiz, *Struct. Bonding* **2004**, *113*, 71-102.

[13] E. Ruiz, A. Rodriguez-Fortea, J. Cano, P. Alemany, *J. Comput. Chem*. **2003**, *24*, 982-989.

[14] H. W. L. Fraser, G. S. Nichol, S. Dey, S. Piligkos, G. Rajaraman, E. K. Brechin, Dalton Trans. **2018**, *47*, 8100-8109.

[15] M. M. Hänninen, A. J. Mota, R. Sillanpää, S. Dey, G. Velmurugan, G. Rajaraman, E. Colacio. *Inorg. Chem*. **2018**, *57*, 3683-3698.

[16] H. Weihe, H.U. Güdel, *J. Am. Chem. Soc*. **1998**, *120*, 2870–2879.

Supporting Information

Synthesis of $[Fe^{III}_{34}(\mu_4\text{-}O)_4(\mu_3\text{-}O)_{34}(\mu\text{-}OH)_{12}Br_{12}(py)_{18}]Br_2$ (1)

$FeBr_3$ (0.591 g, 2 mmol), hexamethylenetetramine (HMTA; 0.476 g, 3.4 mmol) and pyridine (1 mL, 12.3 mmol) were dissolved in MeCN (25 mL). The reaction was left for 2h 45mins with continuous stirring at room temperature. The resulting solution was filtered and left to stand overnight, during which time a small amount of precipitate formed. The precipitate was filtered off and the supernatant layered with acetone. After two weeks, this yielded dark brown, rod-shaped crystals suitable for X-ray diffraction. Anal. Calcd (%) for $C_{90}H_{102}Br_{14}Fe_{34}N_{18}O_{50}$: C 20.58, H 1.96, Fe 36.14, N 4.80; found: C 19.98, H 2.01, Fe 35.88, N 4.52.

Compound **1** can also be prepared by replacing the HMTA in the above reaction with morpholine (4 mmol) or N-methylmorpholine (4 mmol).

X-ray crystallography

Diffraction data for **1** was collected using a Rigaku Oxford Diffraction SuperNova diffractometer with CuK_α radiation, and is given in Table S1. An Oxford Cryosystems Cryostream 700+ low temperature device was used to maintain a crystal temperature of 120.0 K. The structure was solved using ShelXT and refined with version ShelXL interfaced through Olex2.[1],[2] All non-hydrogen atoms were refined using anisotropic displacement parameters. H atoms were placed in calculated positions geometrically and refined using the riding model. CCDC: 1900069.

Magnetic Susceptibility and Magnetisation (<7 T)

Dc susceptibility and magnetisation data were measured on powdered, polycrystalline samples of **1** in the T = 2-300 K and B = 0-7 T temperature and field ranges on a Quantum Design MPMS XL SQUID magnetometer equipped with a 7 T dc magnet. Diamagnetic corrections were applied to the data using Pascal's constants. A unit cell check of the crystals was performed prior to measurement.

High Field Pulsed Magnetisation (<35 T)

Low-temperature magnetisation data was measured by the use of a conventional inductive probe in pulsed-magnetic fields, where the temperature reached as low as 1.6 K.[3] The maximum field reached was 35 T. Polycrystalline samples with a typical mass of 15 mg were mounted in a capillary tube made of polyimide. The sample, which was not fixed within the sample tube, was aligned along the magnetic field direction. Magnetisation curves were found to be identical after we applied the magnetic field several times due to the saturation of the orientation effect.

Heat Capacity

Heat capacity data were collected in the temperature range 0.3–20 K using a Quantum Design PPMS equipped with a ^{3}He cryostat. The powdered, polycrystalline sample of **1** was pressed into a thin pellet

with mass of about 0.5 mg. Apiezon-N grease was used to facilitate the sample thermalization at low temperatures, and its contribution to the heat capacity was subtracted using a phenomenological expression.

High Field, High Frequency EPR (HFEPR)

The HFEPR spectrum for polycrystalline samples was obtained on the Terahertz ESR Apparatus (TESRA-IMR) installed in the magnetism division of Institute of Material Research, Tohoku University.[4] A case made of polyethylene were use for packing the sample. The radiation was produced by Gunn oscillators and backward traveling wave oscillators (BWO).

Table S1. Crystallographic information for **1**.

Compound	**[Fe_{34}] (1)**
Formula	$C_{95}H_{107}Br_{14}Fe_{34}N_{19}O_{50}$
$D_{calc.}$/ g cm^{-3}	1.777
μ/mm^{-1}	22.968
Formula Weight	5332.63
Colour	dark red
Shape	block
Size/mm^3	0.45×0.21×0.17
T/K	120.0
Crystal System	monoclinic
Space Group	$P2_1/n$
a/Å	18.4222(5)
b/Å	32.8959(10)
c/Å	33.9586(9)
α/°	90
β/°	104.444(3)
γ/°	90
V/Å^3	19928.9(10)
Z	4
Z'	1
Wavelength/Å	1.54184
Radiation type	CuK_α
Θ_{min}/°	3.378
Θ_{max}/°	68.251
Measured Refl.	297235
Independent Refl.	36505
Reflections Used	23404
R_{int}	0.2035
Parameters	1897
Restraints	120
Largest Peak	2.270
Deepest Hole	-1.311
GooF	0.995
wR_2 (all data)	0.2880
wR_2	0.2598
R_1 (all data)	0.1309
R_1	0.1044

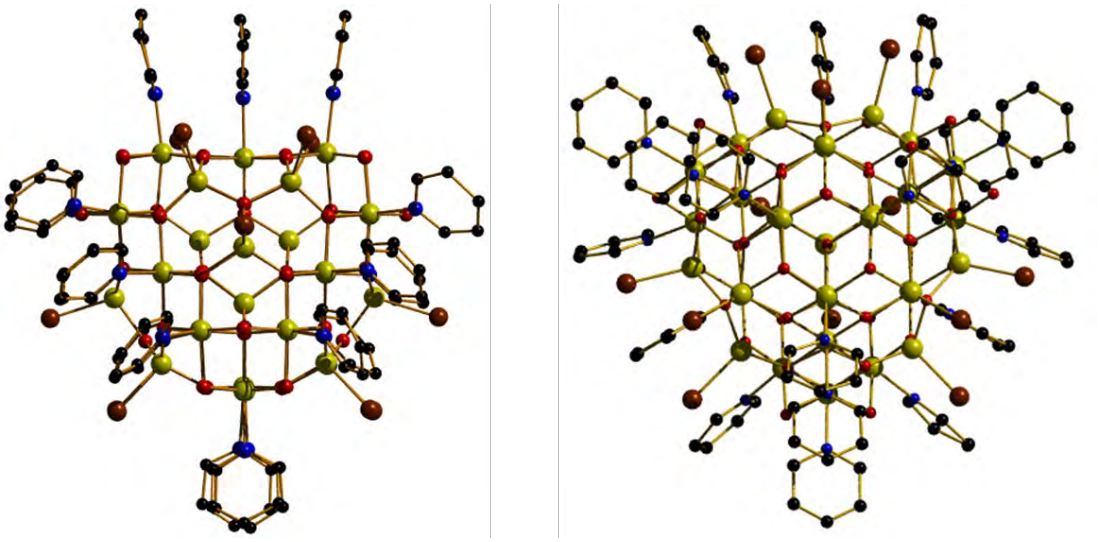

Figure S1. Orthogonal views of the [Fe_{34}] cation. Colour code: Fe = yellow, O = red, C = black, N = blue, Br = brown. H-atoms omitted for clarity.

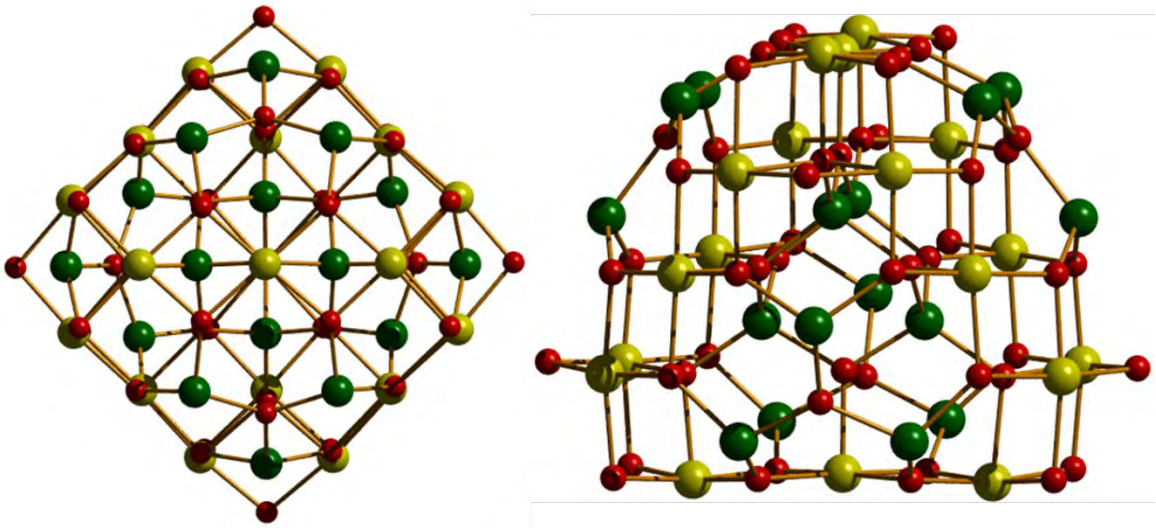

Figure S2. Orthogonal views of the metal-oxygen core of the [Fe_{34}] cation, highlighting the positions of the octahedral (yellow) and tetrahedral (green) Fe ions, and the bridging O (red) atoms.

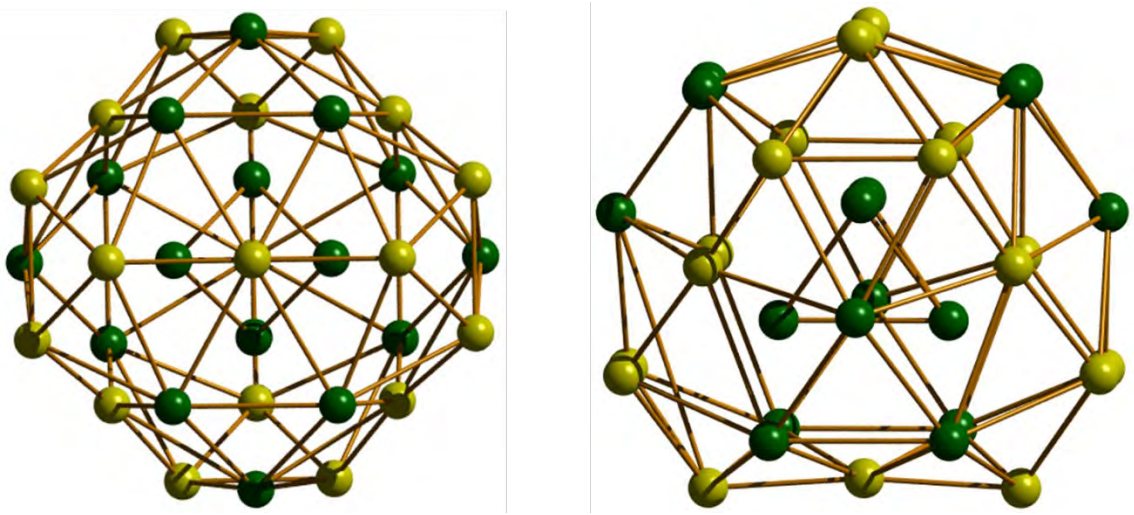

Figure S3. Orthogonal views of the [Fe_{34}] metal polyhedron, highlighting the positions of the octahedral (yellow) and tetrahedral (green) Fe ions.

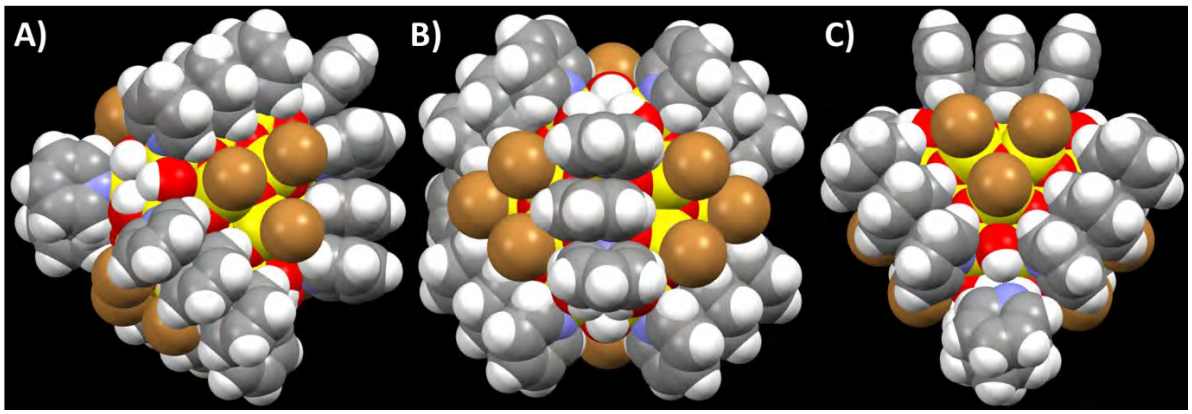

Figure S5. Structure of the [Fe_{34}] cation in **1** in space-fill representation, viewed along the *a*-, *b*- and *c*-axis directions of the unit cell (left-right).

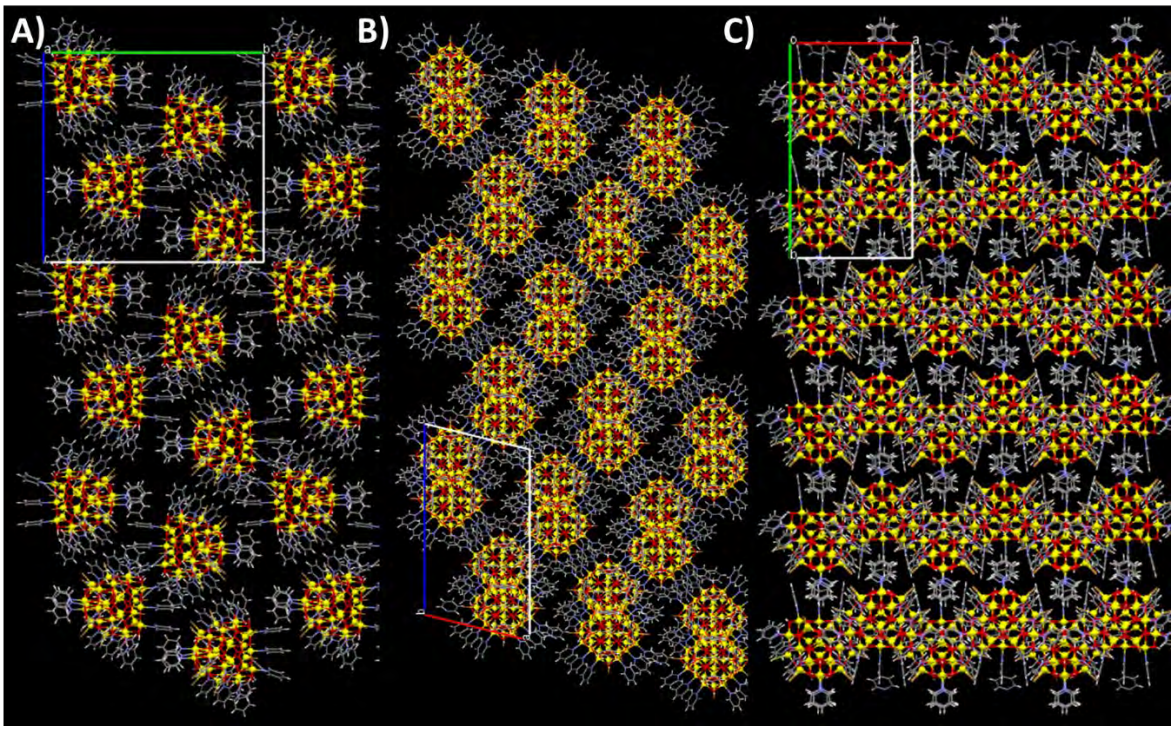

Figure S5. Crystal packing diagram showing the extended structure in **1** in ball-and-stick representation viewed down the *a*-, *b*-, and *c*-axes of the unit cell (left-right). Br counter anions omitted.

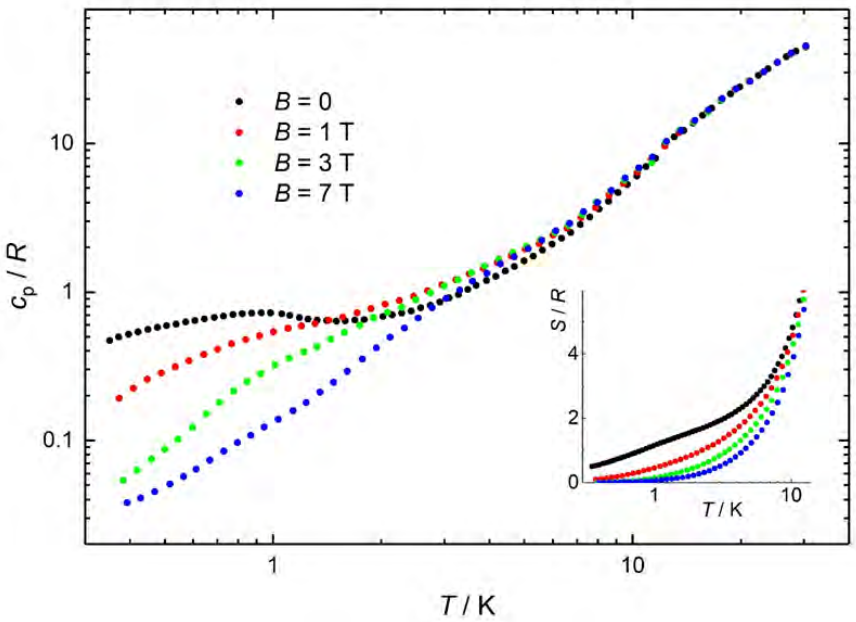

Figure S6: Temperature dependence of the low-temperature experimental heat capacity, c_p/R, and entropy, $S/R = \int c_p/R dT$ (inset), normalized to the gas constant, R, for selected values of the applied magnetic field, B, as labelled. In agreement with the susceptibility data (Fig. 4), both sets of data become field-dependent on lowering the temperature below ca. 10 K, weakly at first and then stronger for $T < 2$ K. In further agreement with the magnetic data, the heat capacity and entropy are very small at the lowest temperatures. For instance, the zero-field magnetic entropy content reaches ca. $S = 1.6\ R$ at $T = 2$ K, which is significantly smaller than that expected for 34 uncoupled Fe^{III} spins, i.e., $S = 34 \times \ln(6) = 60.9\ R$.

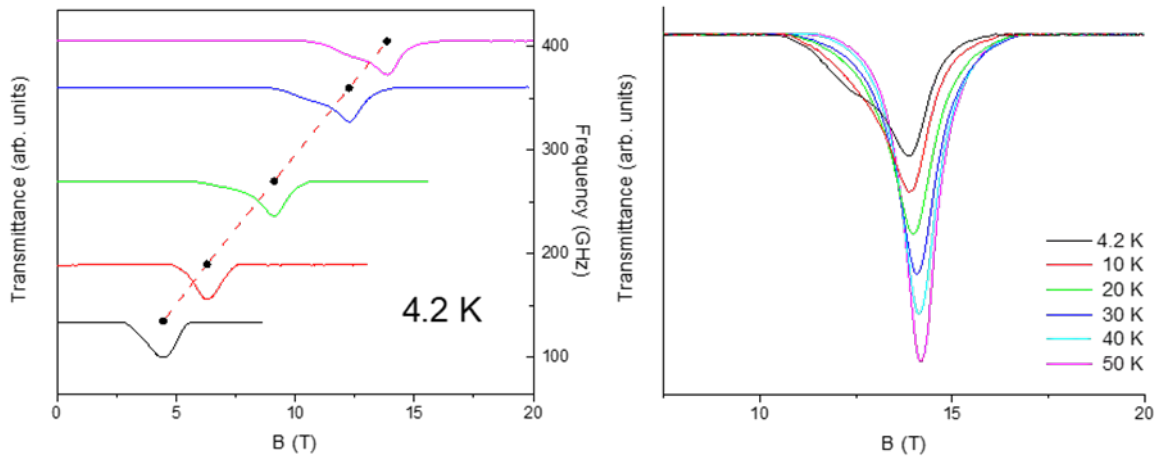

Figure S7: (left) HFEPR spectra of a polycrystalline sample of 1 recorded at 4.2 K and frequencies between 135-405 GHz (left). A linear fit of field-frequency plot gave a *g*-value of 2.04 ± 0.01, and extrapolation of the field-frequency plot gave a zero field resonance frecuency of 8.10 GHz (0.26 cm^{-1}). (right) HFEPR spectra at 405 GHz and tempearatures between 4.2 - 50 K, revealing a narrowing and shift of the resonance field position to higher field with increasing temperature.

Computational Details

We have used the diamagnetic substitution method to calculate the exchange coupling constants in **1** employing the Gaussian 09 suite.[5] Since the calculation on the full structure of **1** is prohibitively expensive and time-consuming, we have divided the Fe_{34} cluster into five model complexes in order to calculate the five exchange coupling constants (J_1-J_5). See Figures S6-S10 below. In these models, the surrounding Fe(III) ions not involved in the pairwise exchange interaction under investigation were substituted by diamagnetic Ga(III) ions in order to maintain the same coordination environment. The exchange coupling constants were estimated using the broken symmetry approach developed by Noodleman.[6] Ahlrichs' triple-ξ plus polarisation basis set was used for the Fe, O, Br and N atoms, while the split valance plus polarisation basis set was used for Ga, C, and H atoms.[7] All theoretical calculations have been performed using the B3LYP functional since it has been proven to produces excellent estimates of *J* values.[8],[9],[10] Exchange coupling constants have been derived from the difference between the broken symmetry and high spin (HS) state, and the quardatic conversion method.

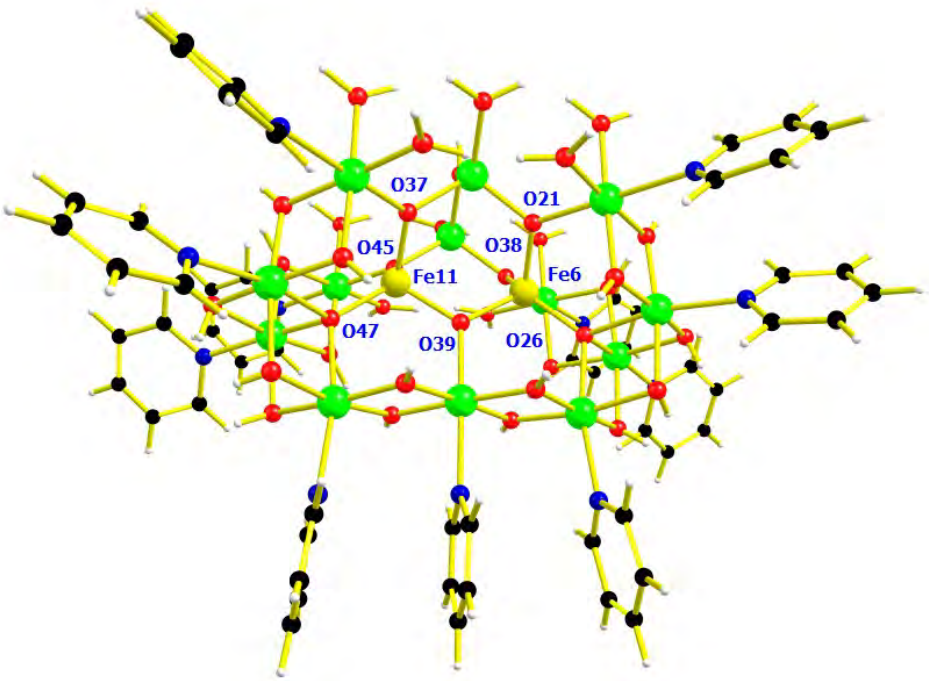

Figure S8. Model structure used to calculate the J_1 exchange. Colour Code: Fe – Yellow; Ga – Green; Br - Brown; O – Red; N – Blue; C – Black; H - White.

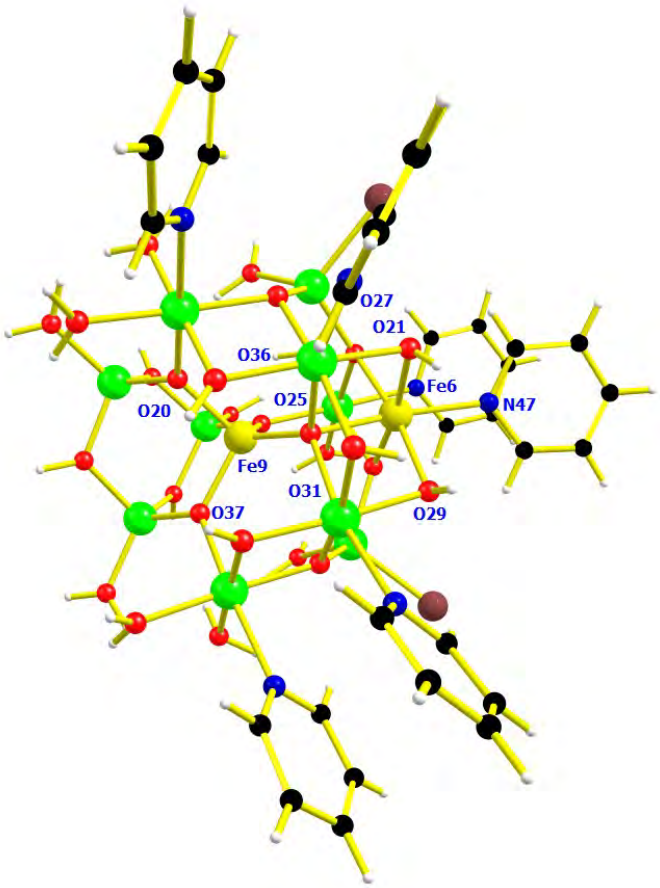

Figure S9. Model structure used to calculate the J_2 exchange. Colour Code: Fe – Yellow; Ga – Green; Br - Brown; O – Red; N – Blue; C – Black; H - White.

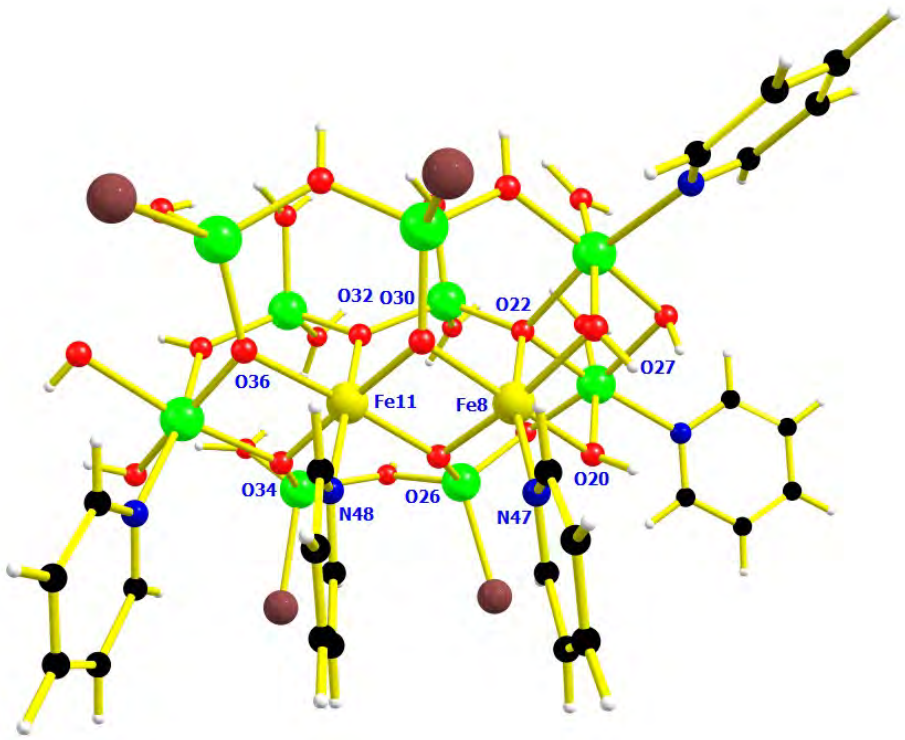

Figure S10. Model structure to calculate the J_3 exchange. Colour Code: Fe – Yellow; Ga – Green; Br - Brown; O – Red; N – Blue; C – Black; H - White.

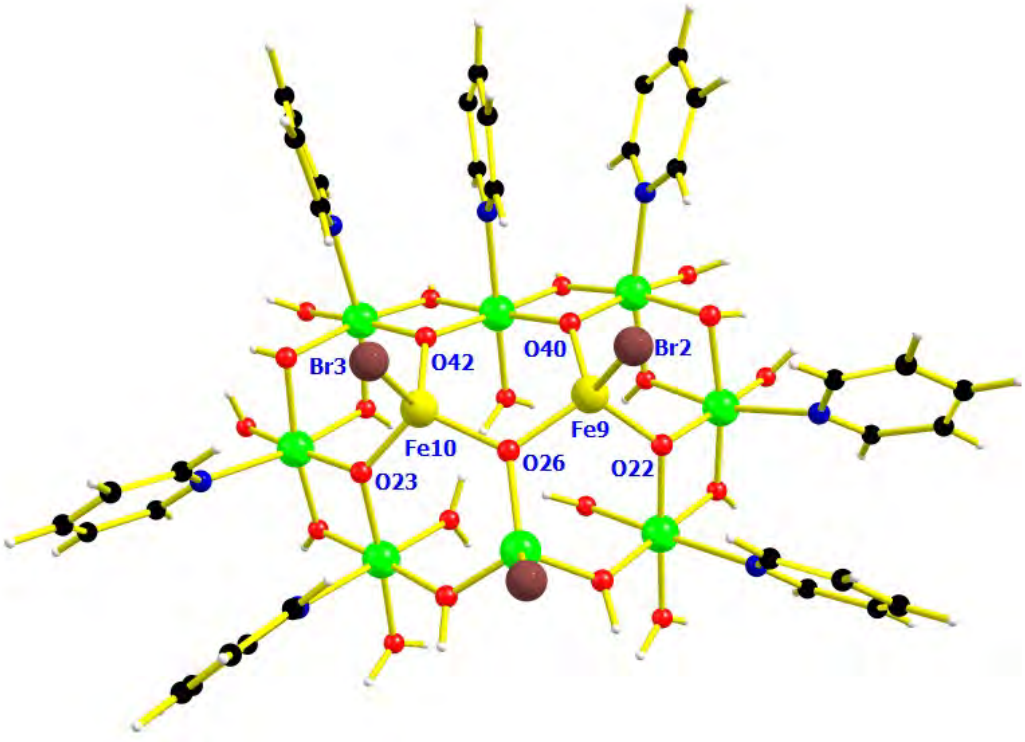

Figure S11. Model structure used to calculate the J_4 exchange. Colour Code: Fe – Yellow; Ga – Green; Br - Brown; O – Red; N – Blue; C – Black; H - White.

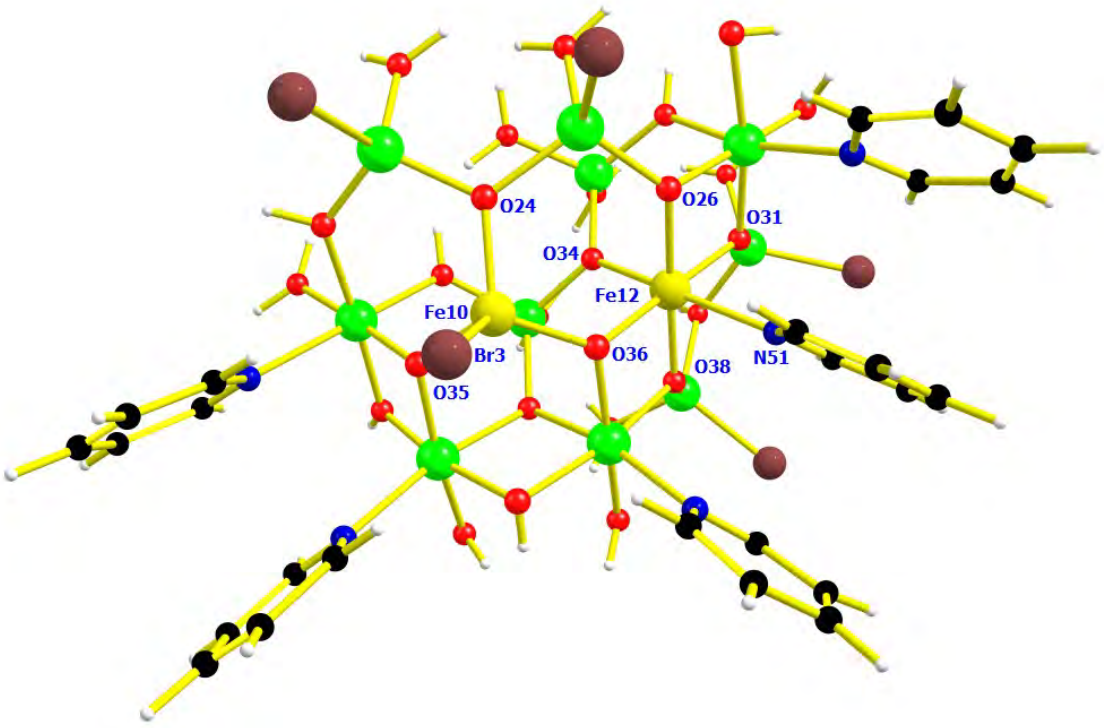

Figure S12. Model structure to calculate the J_5 exchange. Colour Code: Fe – Yellow; Ga – Green; Br - Brown; O – Red; N – Blue; C – Black; H - White.

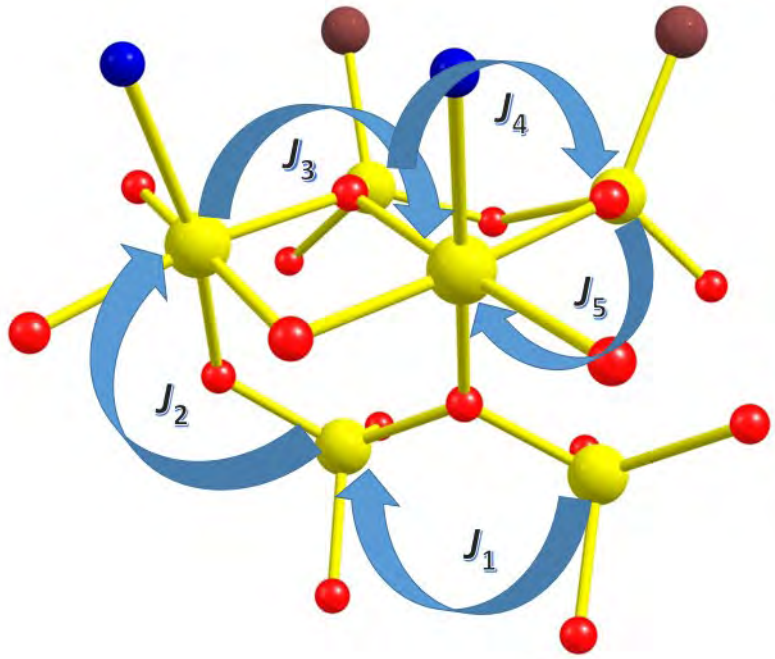

$$\hat{H} = -6J_1\left[\hat{S}_{Itd} - \hat{S}_{Itd}\right] - 24J_2\left[\hat{S}_{Itd} - \hat{S}_{oct}\right] - 25J_3\left[\hat{S}_{oct} - \hat{S}_{oct}\right] - 12J_4\left[\hat{S}_{Otd} - \hat{S}_{Otd}\right] - 48J_5\left[\hat{S}_{Otd} - \hat{S}_{oct}\right] \quad (1)$$

$$H = -J_1\left[\widehat{S_1}\hat{S}_2 + \hat{S}_1\hat{S}_3 + \widehat{S_1}\hat{S}_4 + \hat{S}_2\hat{S}_4 + \hat{S}_2\hat{S}_3 + \hat{S}_3\hat{S}_4\right] - J_2\left[\hat{S}_1\hat{S}_8 + \hat{S}_1\hat{S}_{34} + \widehat{S_1}\hat{S}_6 + \widehat{S_1}\hat{S}_5 + \widehat{S_1}\hat{S}_{10} + \hat{S}_{17} + \hat{S}_2\hat{S}_{27} + \hat{S}_2\hat{S}_{28} + \hat{S}_2\hat{S}_{31} + \hat{S}_2\hat{S}_{30} + \hat{S}_2\hat{S}_5 + \hat{S}_2\hat{S}_{25} + \hat{S}_3\hat{S}_{12} + \hat{S}_3\hat{S}_{13} + \hat{S}_3\hat{S}_{14} + \hat{S}_3\hat{S}_{10} + \hat{S}_3\hat{S}_{25} + \hat{S}_3\hat{S}_{22} + \hat{S}_4\hat{S}_{19} + \hat{S}_4\hat{S}_{20} + \hat{S}_4\hat{S}_{21} + S_4\hat{S}_{17} + \hat{S}_4\hat{S}_{30} + \hat{S}_4\hat{S}_{22}\right] - J_3\left[\hat{S}_{31}\hat{S}_{28} + \hat{S}_{28}\hat{S}_{30} + \hat{S}_{30}\hat{S}_{20} + \hat{S}_{20}\hat{S}_{21} + \hat{S}_{21}\hat{S}_{22} + \hat{S}_{22}\hat{S}_{13} + \hat{S}_{13}\hat{S}_{14} + \hat{S}_{13}\hat{S}_{12} + \hat{S}_{14}\hat{S}_{12} + \hat{S}_{14}\hat{S}_{10} + \hat{S}_{10}\hat{S}_8 + \hat{S}_8\hat{S}_6 + \hat{S}_8\hat{S}_{34} + \hat{S}_6\hat{S}_5 + \hat{S}_5\hat{S}_{31} + \hat{S}_{34}\hat{S}_9 + \hat{S}_{31}\hat{S}_{27} + +\hat{S}_{34}\hat{S}_{17} + \hat{S}_{28}\hat{S}_{27} + \hat{S}_{27}\hat{S}_{25} + \hat{S}_{25}\hat{S}_{12} + \hat{S}_{19}\hat{S}_{17} + \hat{S}_{19}\hat{S}_{20} + \widehat{S_{19}}\hat{S}_{21} + \hat{S}_6\hat{S}_{34}\right] - J_4\left[\hat{S}_7\hat{S}_{11} + \hat{S}_7\hat{S}_{26} + \hat{S}_{11}\hat{S}_{26} + \hat{S}_{18}\hat{S}_{33} + \hat{S}_{18}\hat{S}_{32} + \hat{S}_{32}\hat{S}_{33} + \hat{S}_9\hat{S}_{16} + \hat{S}_9\hat{S}_{15} + \hat{S}_{15}\hat{S}_{16} + \hat{S}_{23}\hat{S}_{24} + \hat{S}_{23}\hat{S}_{29} + S_{24}\hat{S}_{29}\right] - J_5\left[\widehat{S_9}\hat{S}_{17} + \widehat{S_9}\hat{S}_{34} + \hat{S}_9\hat{S}_8 + \hat{S}_9\hat{S}_{10} + \hat{S}_{16}\hat{S}_{17} + \hat{S}_{16}\hat{S}_{19} + \hat{S}_{16}\hat{S}_{21} + \hat{S}_{16}\hat{S}_{22} + \hat{S}_{15}\hat{S}_{10} + \hat{S}_{15}\hat{S}_{14} + \hat{S}_{15}\hat{S}_{22} + \hat{S}_{15}\hat{S}_{13} + \hat{S}_7\hat{S}_8 + \hat{S}_7\hat{S}_{10} + \hat{S}_7\hat{S}_6 + \hat{S}_7\hat{S}_5 + \hat{S}_{11}\hat{S}_{12} + \hat{S}_{11}\hat{S}_{25} + \hat{S}_{11}\hat{S}_{14} + \hat{S}_{11}\hat{S}_{10} + \hat{S}_{26}\hat{S}_{25} + \hat{S}_{26}\hat{S}_{27} + \hat{S}_{26}\hat{S}_5 + \hat{S}_{26}\hat{S}_{31} + \hat{S}_{32}\hat{S}_{28} + \hat{S}_{32}\hat{S}_{30} + \hat{S}_{32}\hat{S}_5 + \hat{S}_{32}\hat{S}_{31} + \hat{S}_{18}\hat{S}_{19} + \hat{S}_{18}\hat{S}_{20} + \hat{S}_{18}\hat{S}_{30} + \hat{S}_{18}\hat{S}_{17} + \hat{S}_{23}\hat{S}_{22} + \hat{S}_{23}\hat{S}_{13} + \hat{S}_{23}\hat{S}_{25} + \hat{S}_{23}\hat{S}_{12} + \hat{S}_{29}\hat{S}_{27} + \hat{S}_{29}\hat{S}_{28} + \hat{S}_{29}\hat{S}_{30} + \hat{S}_{29}\hat{S}_{25} + \hat{S}_{24}\hat{S}_{20} + \hat{S}_{24}\hat{S}_{30} + \hat{S}_{24}\hat{S}_{21} + \hat{S}_{24}\hat{S}_{22} + \hat{S}_{33}\hat{S}_{17} + \hat{S}_{33}\hat{S}_{34} + \hat{S}_{33}\hat{S}_6 + \hat{S}_{33}\hat{S}_5\right] \quad (2)$$

Scheme S1. Schematic of the five different exchange interactions present in **1**, together with the exchange part of the corresponding spin-Hamiltonian (1), and the expanded total exchange spin Hamiltonian (2). $\hat{S}_{Itd}$ is the spin operator of the inner tetrahedral ions, $\hat{S}_{oct}$ the octahedral ions, and $\hat{S}_{Otd}$ the outer tetrahedral ions.

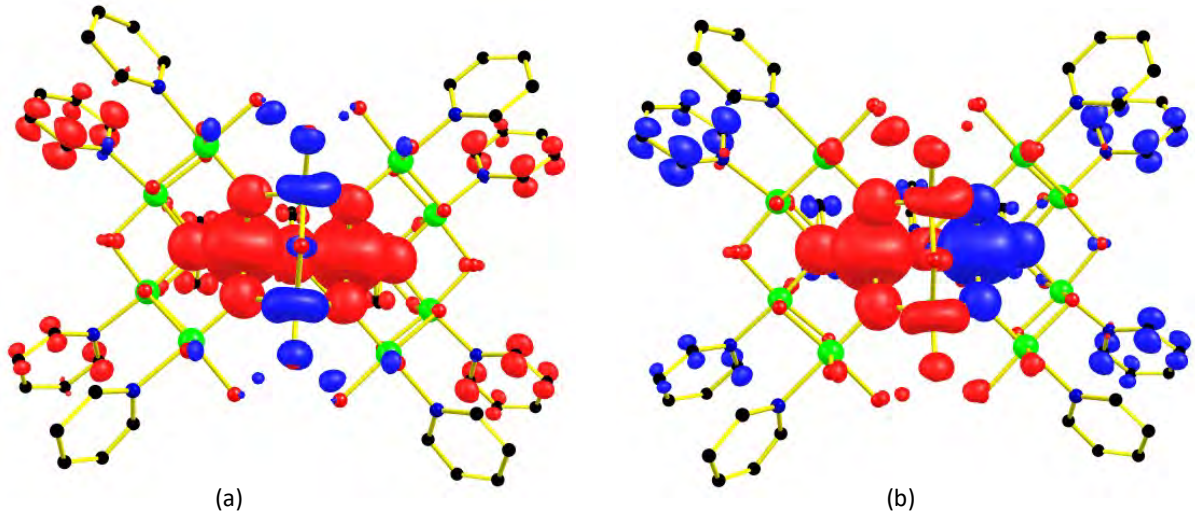

(a) (b)

Figure S13: Spin density plots for the J_1 model complex exchange pathway; (a) High Spin, (b) Broken Symmetry. The isodensity surface shown corresponds to a value of 0.003 e -/bohr^3. The red and blue surfaces represent positive and negative spin density, respectively. Colour Code: Fe – Yellow; Ga – Green; Br - Brown; O – Red; N – Blue; C – Black. Hydrogen atoms are omitted for clarity.

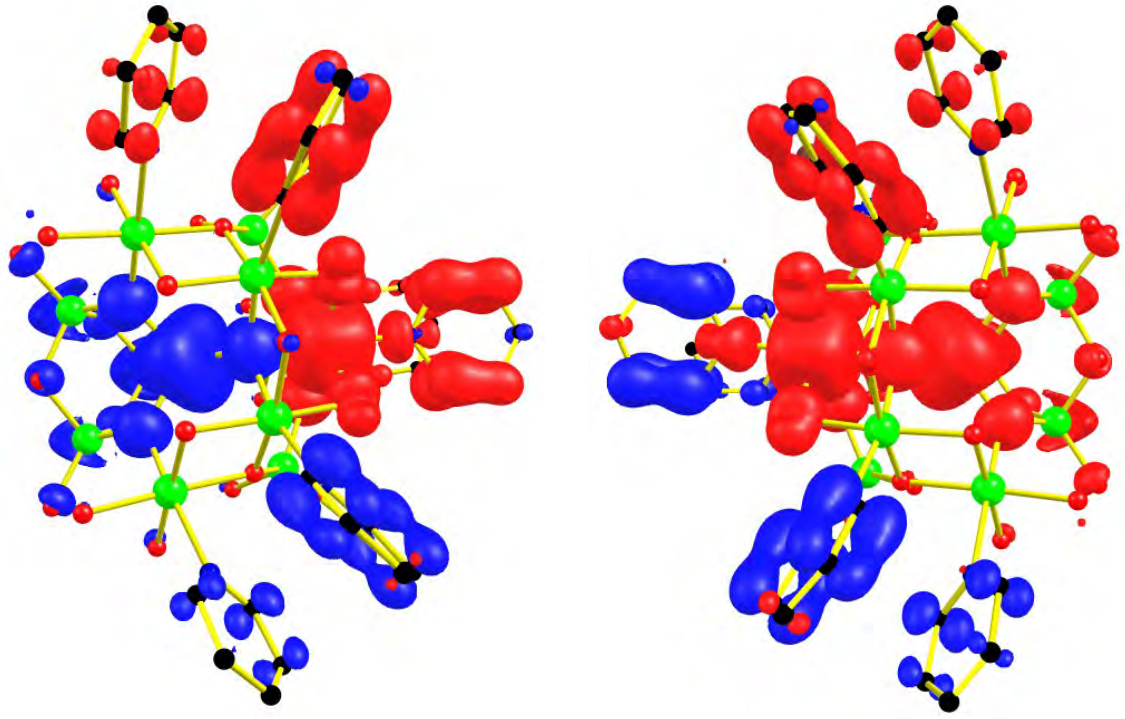

(a) (b)

Figure S14: Spin density plots for the J_2 model complex exchange pathway; (a) High Spin, (b) Broken Symmetry. The isodensity surface shown corresponds to a value of 0.003 e -/bohr^3. The red and blue surfaces represent positive and negative spin density, respectively. Colour Code: Fe – Yellow; Ga – Green; Br - Brown; O – Red; N – Blue; C – Black. Hydrogen atomss are omitted for clarity.

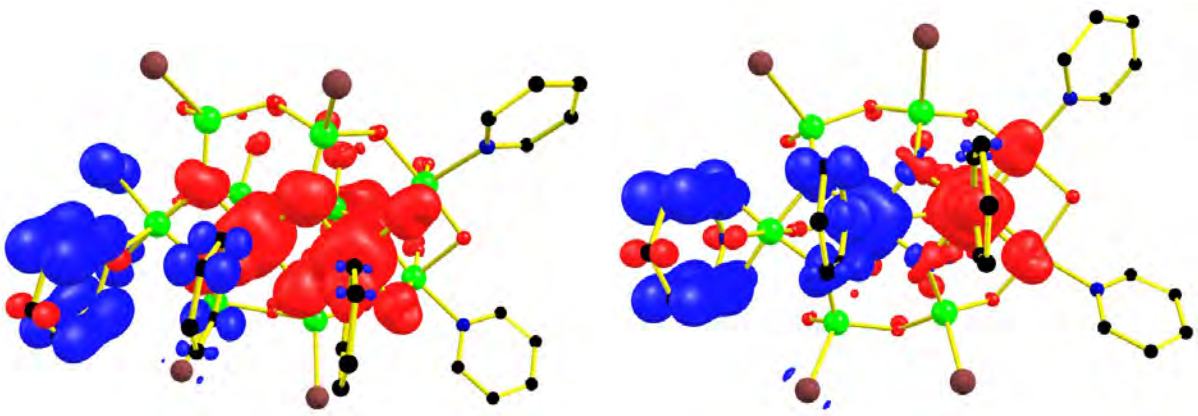

(a) (b)

Figure S15: Spin density plots for the J_3 model complex exchange pathway; (a) High Spin, (b) Broken Symmetry. The isodensity surface shown corresponds to a value of 0.003 e -/bohr^3. The red and blue surfaces represent positive and negative spin density, respectively. Colour Code: Fe – Yellow; Ga – Green; Br - Brown; O – Red; N – Blue; C – Black. Hydrogen atoms are omitted for clarity.

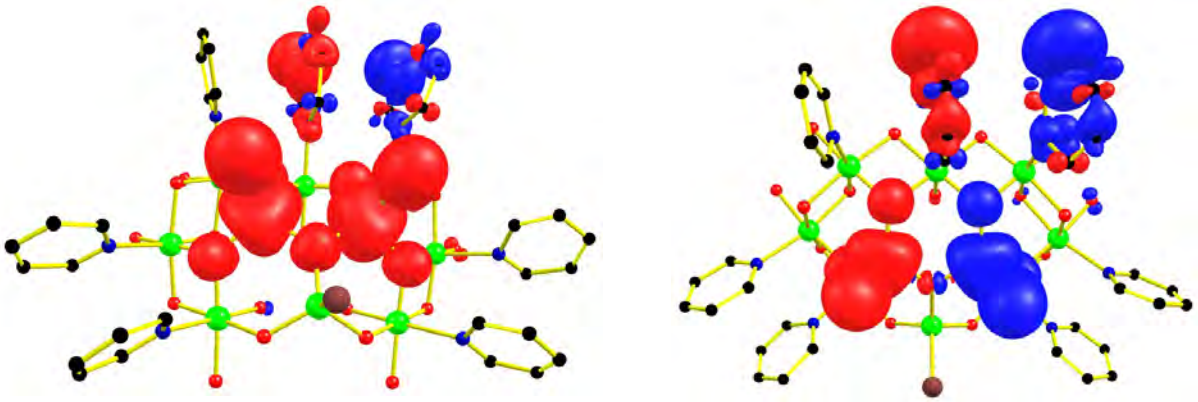

(a) (b)

Figure S16: Spin density plots for the J_4 model complex exchange pathway; (a) High Spin, (b) Broken Symmetry. The isodensity surface shown corresponds to a value of 0.003 e -/bohr^3. The red and blue surfaces represent positive and negative spin density, respectively. Colour Code: Fe – Yellow; Ga – Green; Br - Brown; O – Red; N – Blue; C – Black. Hydrogen atoms are omitted for clarity.

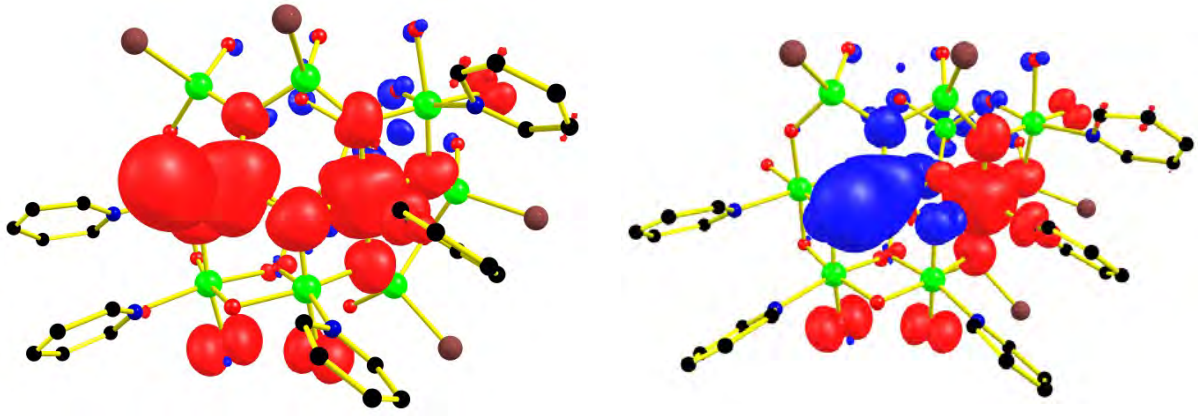

(a) (b)

Figure S17: Spin density plots for the J_5 model complex exchange pathway; (a) High Spin, (b) Broken Symmetry. The isodensity surface shown corresponds to a value of 0.062 e -/bohr^3. The red and blue surfaces represent positive and negative spin density, respectively. Colour Code: Fe – Yellow; Ga – Green; Br - Brown; O – Red; N – Blue; C – Black. Hydrogens are omitted for clarity.

Table S2. The Mulliken spin density of the atoms surrounding the Fe(III) centre in the J_1 exchange pathway (see the atom numbering in Figure S6).

Atom	HS	BS
Fe6	4.077	-4.015
Fe11	4.090	4.134
O39	0.406	0.085
O37	0.121	0.127
O47	0.206	0.227
O45	0.122	0.130
O26	0.202	-0.183
O21	0.118	-0.108
O38	0.115	-0.106

Table S3. The Mulliken spin density of the atoms surrounding the Fe(III) centre in the J_2 exchange pathway (see the atom numbering in Figure S7).

Atom	HS	BS
Fe6	4.286	4.266
Fe9	4.006	-4.002
O25	0.286	-0.156
O29	0.107	0.091
O27	0.136	0.127
O21	0.124	0.110
O31	0.129	0.119
N47	0.146	0.031
O36	0.104	-0.102
O37	0.108	-0.108
O20	0.106	-0.106

Table S4. The Mulliken spin density of the atoms surrounding the Fe(III) centre in the J_3 exchange pathway (see the atom numbering in Figure S8).

Atom	HS	BS
Fe8	4.252	4.250
Fe11	4.253	-4.256
O26	0.273	0.029
O30	0.263	0.018
O20	0.111	0.108
O27	0.132	0.130
O22	0.058	0.055
N47	0.111	0.110
O34	0.132	-0.124
O36	0.132	-0.122
N48	0.109	-0.069
O32	0.054	-0.015

Table S5. The Mulliken spin density of the atoms surrounding the Fe(III) centre in the J_4 exchange pathway (see the atom numbering in Figure S9).

Atom	HS	BS
Fe9	4.095	-4.074
Fe10	4.088	4.072
O26	0.202	0.001
O23	0.187	0.186
O42	0.243	0.242
Br3	0.312	0.307
O40	0.236	-0.232
O22	0.181	-0.178
Br2	0.321	-0.315

Table S6. The Mulliken spin density of the atoms surrounding the Fe(III) centre in the J_5 exchange pathway (see the atom numbering in Figure S10).

Atom	HS	BS
Fe10	4.081	-4.051
Fe12	4.259	4.222
O36	0.365	-0.082
O38	0.122	0.117
O31	0.111	0.109
O26	0.119	0.115
O34	0.016	0.013
N51	0.091	0.090
O35	0.184	-0.185
O24	0.076	--0.079
Br3	0.351	-0.343

Table S7. Overlap integral between the 3d orbitals of the Fe(III) ions in the J_1 exchange pathway. The most significant are highlighted in yellow.

Beta→ Alpha	d_{z^2}	d_{xy}	d_{xz}	$d_{x^2-y^2}$	d_{yz}
d_{yz}	0.175	-0.027	0.175	-0.000	-0.234
d_{xy}	0.021	0.041	0.076	0.041	-0.082
d_{z^2}	-0.073	0.013	-0.144	-0.093	-0.216
$d_{x^2-y^2}$	-0.066	0.063	-0.024	-0.331	0.058
d_{xz}	-0.262	0.003	-0.143	0.153	-0.058

Table S8. Overlap integral between the 3d orbitals of the Fe(III) ions in the J_2 exchange pathway. The most significant are highlighted in yellow.

Beta→ Alpha	d_{yz}	$d_{x^2-y^2}$	d_{xy}	d_{xz}	d_{z^2}
$d_{x^2-y^2}$	0.141	-0.007	0.184	-0.236	-0.098
d_{yz}	-0.033	0.319	0.081	-0.202	-0.151
d_{xz}	0.123	0.196	0.062	0.036	-0.270
d_{xy}	0.117	-0.089	-0.103	0.243	0.282
d_{z^2}	-0.013	0.071	0.035	-0.113	0.099

Table S9. Overlap integral between the 3d orbitals of the Fe(III) ions in the J_3 exchange pathway. The most significant are highlighted in yellow.

Beta→ Alpha↓	d_{xz}	d_{xy}	d_{yz}	$d_{x^2-y^2}$	d_{z^2}
d_{xz}	0.021	0.011	-0.003	0.014	-0.044
d_{xy}	-0.041	0.197	-0.047	-0.036	-0.121
d_{yz}	-0.110	-0.002	-0.158	0.045	-0.178
$d_{x^2-y^2}$	-0.027	-0.317	-0.081	-0.171	-0.068
d_{z^2}	-0.106	0.047	0.031	-0.012	-0.017

Table S10. Overlap integral between the 3d orbitals of the Fe(III) ions in the J_4 exchange pathway. The most significant are highlighted in yellow.

Beta→ Alpha	d_{z^2}	d_{xz}	d_{yz}	d_{xy}	$d_{x^2-y^2}$
d_{z^2}	0.264	0.266	-0.037	0.032	0.103
d_{xy}	0.077	0.053	0.024	0.018	-0.008
d_{xz}	-0.068	0.119	0.119	-0.285	-0.177
$d_{x^2-y^2}$	0.014	0.000	0.364	-0.113	0.001
d_{yz}	-0.012	-0.038	-0.087	0.019	-0.213

Table S11. Overlap integral between the 3d orbitals of the Fe(III) ions in the J_5 exchange pathway. The most significant are highlighted in yellow.

Beta→ Alpha↓	d_{x2-y2}	d_{yz}	d_{xz}	d_{xy}	d_{z^2}
d_{z2}	0.106	0.220	0.262	0.025	-0.011
d_{xy}	0.071	-0.007	-0.011	-0.148	-0.005
$d_{x^2-y^2}$	-0.136	0.223	0.238	0.013	-0.002
d_{yz}	-0.002	0.054	0.212	-0.073	0.027
d_{xz}	-0.005	0.117	0.278	-0.055	-0.264

References

[1] G. M. Sheldrick, *Acta Crystallogr. Sect. C: Cryst. Struct. Commun.* **2015**, *71*, 3-8.

[2] O. V. Dolomanov, L. J. Bourhis, R. J. Gildea, J. A. K. Howard, H. Puschmann, *J. Appl. Crystallogr.* **2009**, *42*, 339-341.

[3] H. Nojiri, K.-Y. Choi, N. Kitamura, *J. Magn. Mater.*, **2007**, *310*, 1468-1472.

[4] H. Nojiri, Y. Ajiro, T. Asano, J.-P. Boucher, *New J. Phys.*, **2006**, *8*, 218.

[5] M. J. Frisch, G. W. Trucks, H. B. Schlegel, G. E. Scuseria, M. A. Robb, J. R. Cheeseman, G. Scalmani, V. Barone, G. A. Petersson, H. Nakatsuji, X. Li, M. Caricato, A. Marenich, J. Bloino, B. G. Janesko, R. Gomperts, B. Mennucci, H. P. Hratchian, J. V. Ortiz, A. F. Izmaylov, J. L. Sonnenberg, D. Williams-Young, F. Ding, F. Lipparini, F. Egidi, J. Goings, B. Peng, A. Petrone, T. Henderson, D. Ranasinghe, V. G. Zakrzewski, J. Gao, N. Rega, G. Zheng, W. Liang, M. Hada, M. Ehara, K. Toyota, R. Fukuda, J. Hasegawa, M. Ishida, T. Nakajima, Y. Honda, O. Kitao, H. Nakai, T. Vreven, K. Throssell, J. A. Montgomery Jr., J. E. Peralta, F. Ogliaro, M. Bearpark, J. J. Heyd, E. Brothers, K. N. Kudin, V. N. Staroverov, T. Keith, R. Kobayashi, J. Normand, K. Raghavachari, A. Rendell, J. C. Burant, S. S. Iyengar, J. Tomasi, M. Cossi, J. M. Millam, M. Klene, C. Adamo, R. Cammi, J. W. Ochterski, R. L. Martin, K. Morokuma, O. Farkas, J. B. Foresman, D. J. Fox, Gaussian 09, Revision A.02, Gaussian Inc., Wallingford CT, **2016**.

[6] L. Noodleman, *J. Chem. Phys*. **1981**, *74*, 5737–5743.

[7] A. Schäfer, C. Huber, R. Ahlrichs, *J. Chem. Phys*. **1994**, *100*, 5829.

[8] D. Becke, *J. Chem. Phys*. **1993**, *98*, 5648–5652.

[9] A. Schäfer, H. Horn, R. Ahlrichs, *J. Chem. Phys*. **1992**, *97*, 2571–2577.

[10] A. Schäfer, C. Huber and R. Ahlrichs, *J. Chem. Phys*. **1994**, *100*, 5829–5835.